Digital mammography image simulation using Monte Carlo

Douglas E. Peplow[a)] and Kuruvilla Verghese
Department of Nuclear Engineering, North Carolina State University, Box 7909, Raleigh, North Carolina 27695

(Received 21 December 1998; accepted for publication 8 December 1999)

Monte Carlo simulations of digital images of the contrast detail phantom and the ACR phantom are presented for two different x-ray digital mammography modalities: a synchrotron mammography system and a next-generation scanning slot clinical system. A combination of variance reduction methods made it possible to simulate accurate images using real pixel dimensions within reasonable computation times. The complete method of image simulation, including a simple detector response model, a simple noise model, and the incorporation of system effects (MTF), is presented. The simulated images of the phantoms show good agreement with images measured on the two systems.
© *2000 American Association of Physicists in Medicine.* [S0094-2405(00)00603-9]

Key words: digital mammography, image simulation, Monte Carlo

I. INTRODUCTION

A rapidly expanding area in medical applications of x rays from synchrotrons[1,2] is synchrotron mammography. Several groups worldwide [for example, in Italy[3,4] and the National Synchrotron Light Source (NSLS) at Brookhaven National Laboratory (BNL) in the U.S.[5]] have been generating exciting results in synchrotron mammography using monoenergetic, parallel, plane-polarized x rays, with a high degree of collimation, long air gaps to reduce x-ray scatter contribution, and even crystal analyzers to virtually eliminate image degradation due to scatter. Diffraction of the transmitted beam from the object using a Bragg or Laue analyzer has been shown to produce images that are unparalleled in clarity and contrast.[6] A group in Russia has been doing similar investigations using x-ray tubes instead of synchrotron beams and generating high quality images.[7] Chapman *et al.*[6] have shown that the transmitted and diffracted images can be coupled to obtain a pure absorption image with imaging details smaller than ever seen before. Simultaneously with the development of synchrotron mammography, next-generation clinical mammography systems with slot geometry and digital detectors[8] have been undergoing clinical trials. Scatter contribution is reduced through the use of a narrow collimator slot and detector array scanned across the object. To quantify the amount of scatter in these two types of modalities, a Monte Carlo study was proposed. In this paper we present the results of a code designed to create accurate simulated images for the study of scatter contributions.

Most of the previous Monte Carlo studies[9–11] have attempted to evaluate mammography systems based on simple studies that quantify the scattered radiation striking the image plane from a slab of material, usually water or Lucite. These studies may show trends with energy or slab thickness correctly, but they do not include the full three-dimensional effects, such as air scatter or edge effects. Recently, Jing, Huda, and Walker[12] studied scanning slot systems using a three-dimensional (3-D) model. However, they only focused on the average scatter-to-primary ratio (S/P) observed in a strip located at the center of the image. Spyrou *et al.*[13] has recently performed some Monte Carlo image simulations but using an analog code that required 18 days to run,[14] even for a very simple phantom and system. What is really needed is a way to determine whether or not objects of certain sizes and densities can be seen in the image produced by the mammography system in question. To answer this, a full 3-D model and an entire accurately simulated image are required.

Full-field image simulation for realistic pixel sizes (50 or 100 μm) using standard Monte Carlo techniques would require prohibitively long computing times. Larger pixel sizes could be used for the purpose of modeling to reduce the times, but the clinical relevancy would be lost. Small objects, such as fibrils or calcifications, would not be discernible when using large pixel sizes. In order to simulate images with accurate pixel sizes in reasonable times, a combination of three variance reduction techniques are implemented.

In Sec. III of the paper we describe the methods used in the Monte Carlo simulation code written to generate images from the synchrotron-based system and from the Fischer Senoscan™, a new digital scanning-slot system that is representative of the next generation of clinical mammography machines. The code is verified by comparison to a large set of published computational results and also to images measured on both systems. The concepts presented in this paper should be applicable also to image simulations using general purpose codes such as MCNP™. In fact, Los Alamos National Laboratory[15,16] is currently investigating the incorporation of image simulation capability within a future version of MCNP™.

By comparing real digital images taken by the synchrotron and the Senoscan™, in this paper we will demonstrate that image simulation by Monte Carlo is possible within reasonable computing times. Hopefully this modeling ability will prove as valuable to mammography and other imaging problems in medical physics as it has proven in many other fields. Our focus in this paper is to show that with the right combination of variance reduction methods, Monte Carlo can be used to simulate accurate images within a reasonable

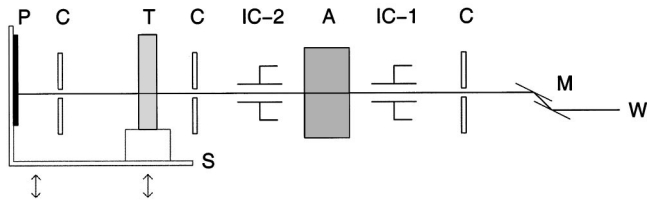

FIG. 1. Imaging with a monoenergetic beam from the synchrotron. The white radiation from the synchrotron (W) passes through the double monochromator (M) to select a single energy of photons. The fan beam is collimated by horizontal slits (C) and the dose is measured by ionization chambers (IC). An absorber (A) is used to attenuate the beam. The stage (S) holding the target object (T) and the image plate (P) are scanned through the fixed beam. Exposure to the plate is regulated by the speed of the stage, which is controlled by the current from the second ionization chamber. (Figure not to scale.)

computing time, which has not been done previously. The detector response and noise models we have used in demonstrating the image simulation capability are simple now but could be improved later.

II. DIGITAL MAMMOGRAPHY SYSTEMS

A. Synchrotron imaging

The new synchrotron-based digital mammography system is still in its early experimental phase of development. The concept is being developed in the United States at the NSLS (BNL) and at the Advanced Photon Source at Argonne National Lab. The basic system consists of a plane-polarized, parallel, monoenergetic source of radiation collimated into a rectangular beam. Since the beam is fixed in position by the monochromator, the object and the imaging plate are scanned through the beam. Since the beam is parallel, there is no geometric magnification and large air gaps are used in addition to various collimators to reduce the amount of scatter. A schematic diagram is shown in Fig. 1.

The system used to take images for this project was on the X15A beamline of the NSLS. The energy of the beam can be selected to be between 18 and 42 keV and the beam size is 13×0.1 cm. The air gap between the target and the image plate is 26 cm. Currently, the image is recorded by a Fuji HR-III image plate and developed by a Fuji BAS2000 image plate reader.

B. Fischer Senoscan™

The Fischer Senoscan™ system, shown schematically in Fig. 2, is a scanning slot system that uses a linear CsI/CCD detector array. The tungsten anode is well collimated and rotates at the same rate as the detector, scanning the breast with a fan beam of x rays in five seconds. Like conventional systems, the x-ray source spectrum consists of bremsstrahlung and it is polyenergetic. The machine can be operated at various kVp settings and has a choice of three filter materials, which greatly reduce the L lines from tungsten.

The machine used for this study was at the University of North Carolina Hospitals as part of the clinical trials for FDA approval, which are currently ongoing at several sites in the U.S. This machine and other digital mammography units are expected to replace the film/screen systems used in clinics today.

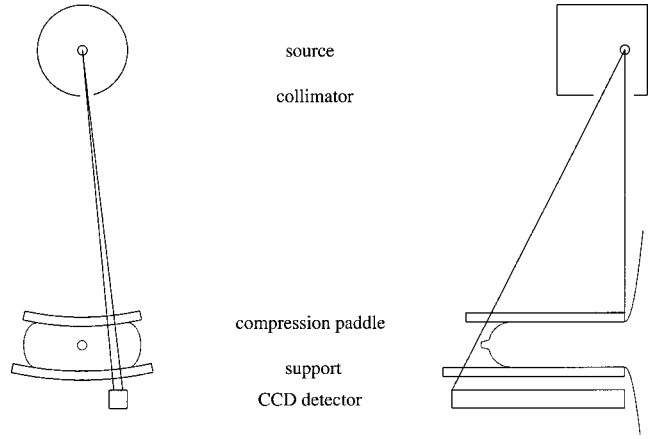

FIG. 2. The Fischer Senoscan™ scanning slot digital mammography unit. The anode and CCD detector array move together scanning the breast with a well-collimated fan beam (Figure not to scale).

C. Mammography phantoms

To compare the two systems, digital images were taken of two very common mammography phantoms—the contrast detail (CD) phantom and the American College of Radiologists (ACR) phantom. The CD phantom is a 1.5 cm thick slab of Lucite with embedded disks of Lucite of varying thicknesses and diameters. Thicknesses range from 0.1 cm down to 0.0063 cm, representing density changes of 7% down to 0.45%. Radii vary from 0.35 to 0.016 cm. Mammography systems are graded on how many objects can be seen in the image. The ACR phantom is a 4.9 cm thick block of Lucite containing a rectangular wax insert with embedded nylon fibers (fibril simulations), aluminum oxide spheres (calcification simulations), and the top portions of plastic balls (tumor simulations). Information pertaining to the placement and composition of the materials of the objects was obtained from the manufacturer, Gammex RMI. Schematics of the two phantoms are shown in Fig. 3.

III. DESCRIPTION OF THE CODE

MCMIS (Monte Carlo Mammography Image Simulation) is a detailed code specifically for the simulation of digital mammography systems, including scanning-slot systems. This code was written so that three variance reduction techniques can be used together. These are source rastering, separation of the scattered and unscattered image, and the point–detector scheme. The code uses four input decks describing the problem, various cross section tables and outputs several image files, image files describing stochastic uncertainty, and tables describing dose and exposure. The code contains four source models, three detector geometries and three detector types. These models and all of their parameters are listed in one of the input decks. The geometry of the object being imaged and a list of materials are listed in other

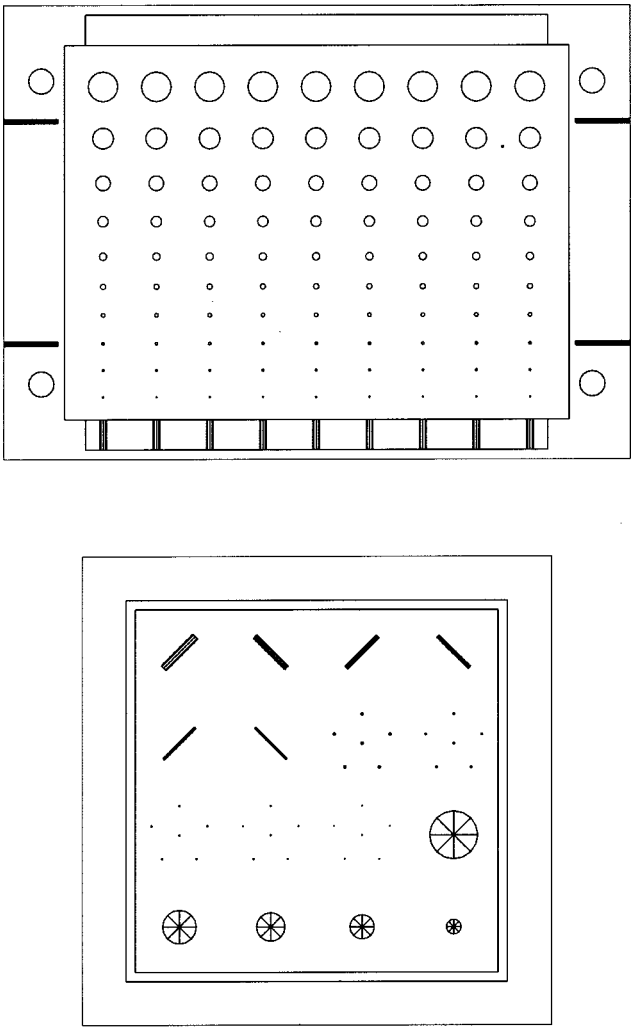

FIG. 3. Schematics of the two common mammography phantoms used in the real and simulated images. The upper drawing is the contrast detail phantom ($10.8\times14.9\times1.5$ cm thick) and the lower drawing is the American College of Radiologists phantom ($10.16\times10.16\times4.88$ cm thick).

input decks. The last input deck contains information for the Monte Carlo run—number of histories, variance reduction methods to use, etc. In addition to the image, this code also calculates for each region the energy deposited, the total flux, the exposure, and the dose.

A. Source models

Four types of monoenergetic sources can be modeled with MCMIS. Polyenergetic sources can be simulated by adding together a set of monoenergetic images weighted by the polyenergetic spectrum, which allows the user to use the same monoenergetic runs to simulate different polyenergetic source spectra. The code is designed in a manner such that sources are at a high z location, pointed down at some target plane. The detector lies on a lower z plane and the image is viewed as a picture with x and y coordinates.

The four source models are the following.

(1) A polarized parallel beam, from a rectangular source rastered over a rectangular target, with a scanning slot oriented in the x direction moving in the y direction. (synchrotron system).
(2) An isotropic point source rastered over a target that is curved in the x direction, with a scanning slot oriented in the y direction moving in the x direction (Fischer system).
(3) A polarized pencil beam, for comparing to other Monte Carlo studies.
(4) An isotropic point source rastered over a flat rectangular target, with a scanning slot oriented in the y direction moving in the x direction. This is also for comparing to other work in the literature.

''Rastering'' refers to the use of a stratified sampling routine used to evenly sample the source over the target area. This is a common variance reduction technique and helps eliminate quantum mottle in the image.

B. Basic transport

The geometry package of MCMIS handles six basic shapes commonly found in phantoms and imaging systems. These are spheres, cylinders (in any orientation), rectangular boxes, boiler plates (curved detector systems), spherical chords (the top of a sphere cut by a plane), and compressed breast shapes (half of a right elliptical cylinder). Geometry regions can be nested to any level. This arrangement makes a description of complex phantoms very simple.

Materials are described by a list of elements: the mass fractions (w_i) of those elements and the density (ρ) of the material. Cross sections are calculated for an energy range of 1 to 300 keV for any material consisting of elements with $Z=1-20$. Photoelectric cross sections are taken from the ITS[17] library and scattering cross sections are calculated by integrating the form factors for the materials. MCMIS has the ability to use either the free-gas atomic form factors[18] or measured molecular form factors[19] for coherent scatter. Incoherent scatter was modeled using atomic incoherent scattering factors.[18]

Interactions modeled in this code include the photoelectric effect, coherent scatter, and incoherent scatter. Implicit capture (forcing a scatter and reducing the weight to account for the fraction that would have been absorbed) and the last-flight estimator variance reduction techniques are available as options. Both of these are well known and will not be discussed here. The code does model polarization effects, if that option is selected by the user, in the scattering interactions. K x-ray fluorescence can be modeled by MCMIS, but this option is not available when using implicit capture since photoelectric events are not simulated.

C. Detector models

In addition to a perfectly absorbing detector designed for use in testing and benchmark problems, two more realistic detectors are modeled by MCMIS. The models for these are still simple but do include some aspects of detector response.

The Fischer Senoscan™ detector is modeled as a CsI plate, 0.015 cm thick. The density and thickness are left to the user as variable inputs and the nominal values used for this report were supplied by Fischer Imaging.[20] The second detector is a photostimulable phosphor imaging plate by Fuji. It is made of $BaFBr_{0.85}I_{0.15}$. Fuji literature with the imaging plate reports values of density thickness of 0.033 g/cm^2 for the HR (high resolution) plate and 0.048 g/cm^2 for ST (standard) plate. Fuji literature also reports a thickness of 0.0150 cm for the phosphor layer.

In order to account for energy deposition across neighboring pixels, energy is deposited along the photon path through the detector layer, weighted by the probability of the photon surviving up to that point in the layer. This is a simple model but more complex than most used in radiographic simulations, which do not consider the spatial distribution of energy at all. Instead of continuing the Monte Carlo game in the detector model, a ray-trace approach is taken. The distance traveled through each pixel is calculated and the probabilities of interaction in those lengths are found. Energy is then distributed according to those probabilities in the pixels the path crosses. A total of $E(1-e^{-\mu t})$ energy is deposited, where μ is the total linear attenuation and t is the total distance through the detector layer. This simplified model does not take into account x-ray fluorescence or electron motion, since that would be contained in the system MTF. The energy deposition of the first interaction of the photon in the detector is included in this model and everything after that is assumed to be in the MTF.

Three types of detector grids are available: a flat plate, a plate curved in the one direction, and a detector made of concentric rings. The synchrotron system uses the flat plate, the Fischer Senoscan™ uses the curved detector and concentric ring model is used for some test problems. Each detector grid type has many parameters set by the user. Scores are split into two images: one for scattered photons and one for unscattered (source) photons.

MCMIS has the unique feature of modeling scanning slot detector motion. Both the synchrotron system and the Fischer Senoscan™ move the source and detector relative to the object being imaged. This motion is modeled by MCMIS by defining a detector slot width (w) and a beam size (b). At the production of each source photon, a line is marked on the detector and the center of the slot is placed randomly within $\pm b/2$ about this line, in the scan direction. Photons that strike the detector region outside the slot are not scored. This scanning slot option may be easily turned off by defining the slot to encompass the entire detector.

D. Variance reduction

For an image of 10 cm by 10 cm with 100 μm pixels (a 1000×1000 array) using 10^7 histories, the number of photons striking any one pixel will be $10\pm\sqrt{10}$. This would be seen in the image as quantum mottle and this amount would completely mask any details in the imaged object. To reduce this mottle to 1%, a total of 10^{10} histories would be needed. Instead, simulating ten histories per pixel (weighted by the angular distribution probability for source emission) will give an image with considerably reduced mottle. This stratified sampling scheme used in Monte Carlo is what we call source rastering.

The path of a photon through a material is picked stochastically from the basic scattering and transport models. At each interaction of the photon there is a small chance of the photon scattering toward a given pixel in the detector, surviving through the material in between the interaction site and that pixel, and then interacting in that pixel. The point–detector scheme calculates this probability for every pixel in the scanning slot of the detector at each interaction that the photon has along its stochastic path. This way, each pixel in the image receives some score with every history instead of just one pixel, where the simulated particle actually strikes. This helps to minimize mottle in the image from scatter. The scheme can also be thought of as a splitting game where the photon is split into many pieces: many that are forced to interact in the pixels of the detector and one that is prevented from striking the detector (the fraction that continues on in the simulation). When the weight of the surviving photon becomes low enough, Russian Roulette is played. Keeping the number of histories per pixel constant, the time required for a simulation is inversely proportional to pixel size raised to the fourth power. Using this scheme for 100 μm pixels in a realistically sized image would result in a prohibitively large simulation time.

To use the point–detector scheme without excessively long computing times, the scattered and unscattered images are computed separately. For the unscattered image, a Monte Carlo simulation is hardly necessary. It can be calculated simply by the exponential attenuation of every material in a line between the source and the target pixel. This is very fast and can be done in a few minutes for a full-field image using 100 μm pixels, allowing the smallest details of the object to be seen in the image. The scattered image does not show small scale structure and can be modeled using larger pixel sizes, which drastically reduces the time required by the point–detector scheme. Pixel sizes up to 0.5 cm were used in this study. The fine mesh unscattered image and the coarse mesh scattered image can then be added together.

IV. TRANSPORT MECHANICS BENCHMARKS

A series of comparisons of the basic parts of our Monte Carlo code package were made against previously published works. This was done to ensure that the fundamental transport, tracking, interaction, and scoring mechanisms in our code worked properly. In this section we will briefly review the comparisons. Detailed graphs and tables of each comparison would require more space than alloted in a journal article and interested readers are referred to the first author's dissertation.[21]

A. Transmission, backscatter, and absorption

For an infinite slab of water, Boone[22] calculated the primary transmission, the total absorption, forward scatter emission, and backward scatter emission of a monoenergetic pen-

cil beam of photons. This was done for a variety of slab thicknesses and primary photon energies. MCMIS was also used to calculate the same quantities and the results agree very closely with Boone's values.

Another check of the transport mechanics used in MCMIS is Boone's calculation of the mean number of scattering events for photons that have escaped the slab. These numbers calculated by MCMIS also compare very well with those from Boone.

B. Scattering distributions

Chan and Doi[10] computed the following for monoenergetic pencil beams of photons hitting a slab of water: angular distributions of scattered photons, as a function of incident photon energy and slab thickness; mean exit angle of scattered photons, as a function of incident photon energy and slab thickness, spectral distributions of scattered photons, as a function of incident photon energy, slab thickness and exit angle; mean energy of scattered photons, as a function of incident photon energy, slab thickness, and exit angle; spectral distributions of scattered photons, as a function of incident photon energy and slab thickness for all exit angles combined; mean energy of photons emerging at any angle, as a function of incident photon energy and slab thickness; numbers of transmitted primary and scattered photons as a function of incident photon energy and slab thickness; and other quantities. MCMIS was used to calculate the same quantities listed above and they all agreed very closely with the results of Chan and Doi. Re-running MCMIS using the measured molecular coherent scattering form factor of water slightly changed the distributions at low angles and low energies.

C. Dose

MCMIS calculates dose by taking the energy deposited in a geometric region and dividing by the mass of the material in that region. Exposure is calculated using a pathlength tally (similar to a total flux tally) but weighted by the energy of the photon and the energy absorption coefficient for air. The code then reports dose or exposure in rads or roentgen, respectively, per photon.

Liu, Goodsitt, and Chan[23] have reported the dose per unit skin entrance exposure for various combinations of kVp settings and spectral HVLs. (The half-value layer is the amount of material required to reduce the exposure in half. This is used as a measure of beam hardness.) In their paper they focus on magnification mammography, but it still provides a useful check. The model used by Liu *et al.* included a divergent point source located 65 cm above the breast support. The breast phantom simulated was a semielliptical right cylinder with a 0.4 cm thick skin made of the same material as the breast. Liu *et al.* calculated the dose per unit entrance exposure as a function of breast thickness for two cases: a standard mammogram and a magnification image. The magnification shot gives the patient a lower dose for the same skin exposure. The ratios computed with MCMIS are 5%–20% lower than those of Liu *et al.* Considering that different cross sections, energy absorption coefficients for air, and different tube spectra were employed, this difference is reasonable. These cases were for 28 kVp without a compression paddle for a 50/50 adipose/glandular tissue breast. Liu reported that their spectrum had a HVL of 0.31 mm Al while the spectrum used in the analysis of the MCMIS data had a HVL of 0.334 mm Al.

MCMIS was also used to calculate the dose per unit entrance exposure for a magnification image on a 100% glandular tissue breast at 30 kVp. Two calculations were made: one without a compression paddle, using a spectrum with a HVL of 0.33 mm Al, and one with a 5 mm Lexan compression paddle, after which the spectrum then had a HVL of 0.42 mm Al. Agreement with the calculation of Liu *et al.* was similar to the above cases.

D. Scanning slot systems S/P

Jing, Huda, and Walker[12] reported in 1998 on the S/P ratio of scanning slot mammography systems. They used the EGS4 Monte Carlo code package to calculate the ratio of energy from scattered radiation absorbed in the detector to energy from the unscattered (primary) radiation. Simulations were for point sources above a Lucite slab ($20\times 20\,\mathrm{cm}^2$ area) and a planar detector (60 cm from the source). Only the center slit was considered. They investigated four parameters: source energy, slab thickness, air gap size between the slab and the detector, and the width of the slot. The molecular coherent scattering form factor reported by Leliveld[24] was used for Lucite. Most simulations were done for a perfectly absorbing detector but a few were performed using a Gd_2O_2S:Tb 36.7 mg/cm^2 plate. They then calculated the S/P ratio over the entire slot for many cases of the four parameters, all to a reported 1% stochastic error. In their paper values for polyenergetic spectra are also reported.

MCMIS was used to simulate 79 of the monoenergetic cases reported by Jing *et al.* The point–detector scheme was turned off and the detector was defined to have one pixel, corresponding to the slot. Scanning motion of the detector and of the slot was not used. All the S/P ratios were calculated to a stochastic error of 1% or less. The results from MCMIS match those of Jing *et al.* very well, typically within 3% of each other, and for a few cases at low energies and small slot widths to within 8%.

V. IMAGE PROCESSING

One run of MCMIS will produce five images—one unscattered image on a fine mesh and four images on a coarse mesh, with both mesh sizes as specified by the user. The four coarse mesh images are an unscattered image, a scattered image, and the stochastic uncertainties from these images. From these images, several steps must be taken to form the final simulated image.

A. Simulation of synchrotron images

The images taken by the synchrotron are not from a truly monoenergetic source and this must be taken into account in simulating an image. Since Bragg reflection of a particular

TABLE I. Energies and intensities (without any filtration) from the monochromator on NSLS beamline X15A. It should be noted that the 1.5–4.5 mm of added aluminum used in the synchrotron images preferentially reduced the low-energy components of the beam.

Desired energy (keV)	[111] reflection E_i (keV)	I_i	[333] reflection E_i (keV)	I_i	[444] reflection E_i (keV)	I_i	[555] reflection E_i (keV)	I_i
18	18	1	54	0.000 65	72	1.7e-6	90	1.9e-7
26	8.67	0.008	26	1	34.67	0.19	43.33	0.016
34	11.33	4.26	34	1	45.33	0.099	56.67	0.0046
42	14	92.80	42	1	56	0.058	70	0.0017

order through a crystal is used to select the energy of the synchrotron beam, reflections of other orders are also present in the beam. For example, for a 26 keV beam selected using the [3,3,3] reflection from a Si crystal, there is a component at 34.67 keV (19% of the intensity of the 26 keV) and a 43.33 keV component (1.6% of the primary intensity). This is easily accounted for in the Monte Carlo calculations by running each component energy and then adding the results weighted by the intensities. The intensities were supplied by the X15A beamline personnel[25] and are shown in Table I.

For each synchrotron image, four monoenergetic components are simulated. The four unscattered images on the fine mesh are added together and the four scattered images on the coarse mesh are added together. The total scattered image is then interpolated using the fine mesh and then added to the total unscattered image creating the total Monte Carlo image. The stochastic uncertainties in the final image were calculated by propagating the stochastic uncertainties in the image components.

To simulate the quantum mottle produced by photon statistics, an appropriate amount of noise (see the next section) is added to the Monte Carlo image. The amount of relative noise for each simulated image was determined by the total flux recorded by the ionization chamber for the corresponding experimental image. The values of relative noise are typically one percent or less.

The next step in the image simulation process is to smear the image with the system MTF. The MTF (modulation transfer function) is the norm of the Fourier transform of the point spread function and describes the spatial resolution of a system. Applying the MTF to an image smears it slightly, taking energy from one pixel and depositing it in the neighboring pixels. This accounts for the smear of the laser light that liberates small amounts of energy from neighboring pixels. In reality, we did not have access to MTF data on this system but we did measure the square-wave response (SWR) with a standard line-pair phantom. Since the SWR and the system MTF are so similar,[26] the SWR was used in place of the MTF. This will not smear the image quite as much as the MTF, but the difference is very slight.

The energy liberated by the laser is in the visible range and there is a quantum mottle associated with it. So, more noise is added to the smeared image making the final simulated image. An example of each stage in this process is shown in Fig. 4. A note about the scattered image—the amount of scatter across this portion of the image—is very constant, not showing any detail. The figure is shown with the contrast maximized, which highlights the statistical variation of a few percent.

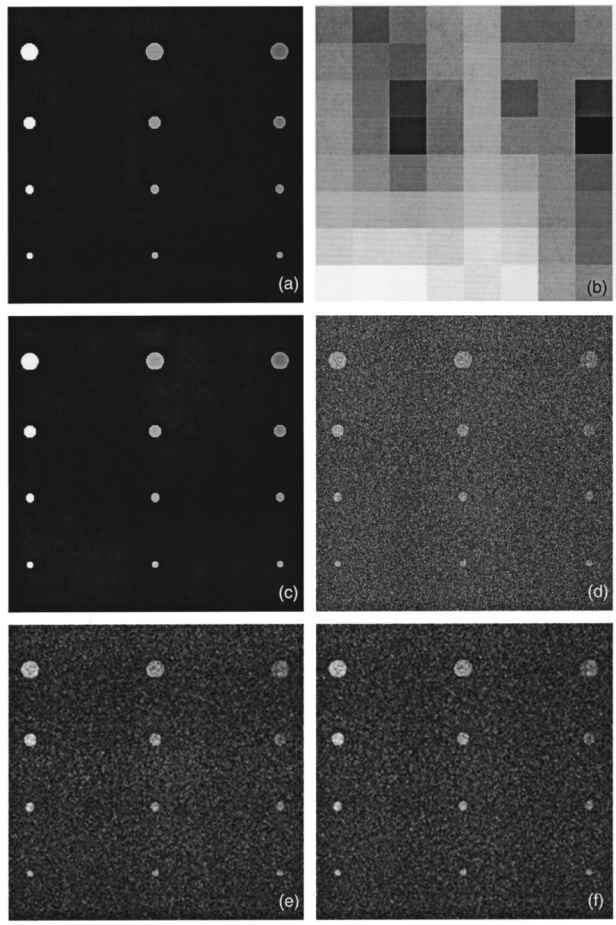

FIG. 4. Image processing for simulating the synchrotron images: (a) the unscattered image and the (b) scattered image calculated by Monte Carlo are added together (c). Quantum mottle noise is then added (d). The image is smeared using the measured system MTF (e) and image plate reader noise is added creating the final image (f). Each image is scaled to maximize visual contrast.

B. Synchrotron imaging noise model

For a good simulation process for the synchrotron, the image noise also needs to be modeled. The simulations are not very useful if one has to take a real image to determine the amount of noise to complete the simulation. By analyzing the noise observed in the 14 synchrotron images and the ionization chamber readings (related to photon flux) for each, a simple noise model was developed.

Noise coming from each step in the image formation process needs to be considered, but the exact amounts and forms are unknown. These steps include the uncertainty associated with the number of photons striking a pixel, the amount of energy deposited in the plate, the number of photons liberated by the laser reading the plate, etc. From the ionization chamber readings before the target, the amount of energy

TABLE II. Parameters of the real and simulated synchrotron images.

#	Phantom	Energy (keV)	Slit width	Real image relative Uncertainty (noise)	Monte Carlo simulations S/P_{mid}	S/P	Unscat. time (hours)	Scat. time (hours)
1	CD	18	3 mm	0.0096	0.0047	0.0037	0.095	2.8
2	CD	26	3 mm	0.0079	0.0036	0.0032	0.064	2.6
3	CD	34	3 mm	0.0070	0.0031	0.0030	0.069	2.7
4	CD	42	3 mm	0.0058	0.0030	0.0027	0.065	2.8
5	CD	18	5 mm	0.0083	0.0063	0.0057	0.060	3.2
6	CD	18	10 mm	0.0091	0.014	0.012	0.039	6.5
7	CD	18	None	0.0078	0.040	0.034	0.008	23.0
8	ACR	18	3 mm	0.0094	0.011	0.010	0.046	4.4
9	ACR	26	3 mm	0.0089	0.010	0.0094	0.044	4.0
10	ACR	34	3 mm	0.0073	0.0092	0.0085	0.038	4.1
11	ACR	42	3 mm	0.0092	0.0090	0.0080	0.037	4.9
12	ACR	18	5 mm	0.0118	0.019	0.018	0.046	6.0
13	ACR	18	10 mm	0.0096	0.040	0.035	0.027	10.5
14	ACR	18	None	0.0119	0.11	0.095	0.016	30.4

striking the image plate, E, can be found. From this, the number of photons is found and then the expected noise from quantum mottle, σ_E, can also be found. When this noise is added to the Monte Carlo image (scattered plus unscattered), the MTF tends to smear it, reducing the relative amount by a factor k. The difference in the relative noise observed in the image and $k\sigma_E/E$ is due to the process of reading the plate, which converts the stored energy into visible photons that are then converted to an electronic signal.

A simple model for the total relative noise (uncertainty) observed in the final image was constructed by proposing that the relative variance of the final image, $(\sigma_I/I)^2$, could be described by the sum of three terms:

$$\left(\frac{\sigma_I}{I}\right)^2=\left(\frac{k\sigma_E}{E}\right)^2+\left(\frac{K_1}{E}\right)^2+(K_2)^2, \tag{1}$$

where the first term represents the amount of quantum mottle as discussed above; the second term represents processes with an error related to the energy deposited in the plate E (for example, the number of light photons generated); and third term represents processes with a constant relative variance.

The two constants K_1 and K_2 were found by fitting the model to the amounts of relative noise observed in the 14 synchrotron images listed in Table II. The results of this noise model are shown in Fig. 5. This model also predicted very well the relative noise in eight other synchrotron images of Lucite and wax phantoms that were not used in finding the two model constants. The measured relative noise levels in these images were between 1% and 1.5% and the model predicted values that followed the trends well and were typically within 10% of the measured values.

The above model for image noise is not intended to be a universal model—it is an empirical model used to fit the noise of the images in our synchrotron imaging system only. This system had the unique ability to measure photon flux through the ionization chambers that most imaging systems do not have. Since the focus of this paper is the Monte Carlo methods, items such as detailed modeling of the CCD or aliasing were not included.

C. Simulation of Senoscan™ images

To simulate polyenergetic images from tube anode systems like the Senoscan™, many monoenergetic runs of MCMIS are required. These runs, made from 5 to 40 keV in 1 keV intervals, are added together, weighted by the tube spectra. For this project, tube spectra from Boone[27] were used.

Quantum mottle noise is added to the image and the system MTF is applied. The MTF accounts for the focal spot size, scanning motion wobble, and x-ray fluorescence in the detector. The MTF was supplied by Fischer Imaging Corporation and checked by an edge-phantom measurement. Of course, the MTF effects and the noise effects are not in re-

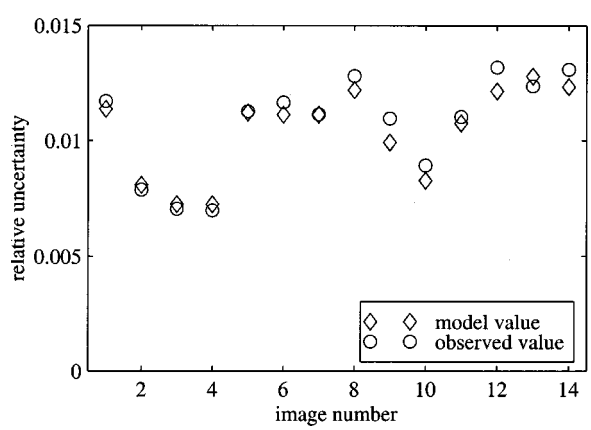

FIG. 5. Predicted relative uncertainty in each synchrotron image using the three-term noise model compared to the observed relative uncertainty in each real image. The 14 images are those listed in Table II.

TABLE III. Parameters of the real and simulated Senoscan™ images.

#	Phantom	kVp	Filter	Real image relative uncertainty (noise)	MC simulations S/P_{mid}	MC simulations S/P
1	CD	25	Al	0.005 29	0.095	0.092
2	CD	30	Al	0.003 82	0.092	0.087
3	CD	35	Al	0.003 93	0.089	0.084
4	CD	30	Rh	0.004 63	0.094	0.090
5	CD	30	Mo	0.006 44	0.096	0.093
6	ACR	30	Al	0.006 51	0.22	0.20
7	ACR	35	Al	0.005 09	0.21	0.19
8	ACR	40	Al	0.004 54	0.19	0.18

ality separate—the best we can do in our simple simulation is to apply them in steps. The Fischer detector system is more complex than what was used for the synchrotron images and the noise was considerably less (see Table III). So, we did not attempt to model the noise for this system. Instead, we used an amount of noise typically seen in the Senoscan™ images of 0.5%. This value was calculated by looking at an area of the image that ought to have had uniform values and finding the variance. For the images taken for this experiment, the values were all between 0.38% and 0.64%, with approximate median values of 0.5%.

Real Fischer images are corrected for the flux falloff toward the nipple by dividing the entire image by the whiteline profile, which is the flux profile recorded at a standard kVp and extra-large filter thickness. This is also done for the simulated image, dividing by a profile generated by a separate Monte Carlo run matching the specifications of the Fischer whiteline image.

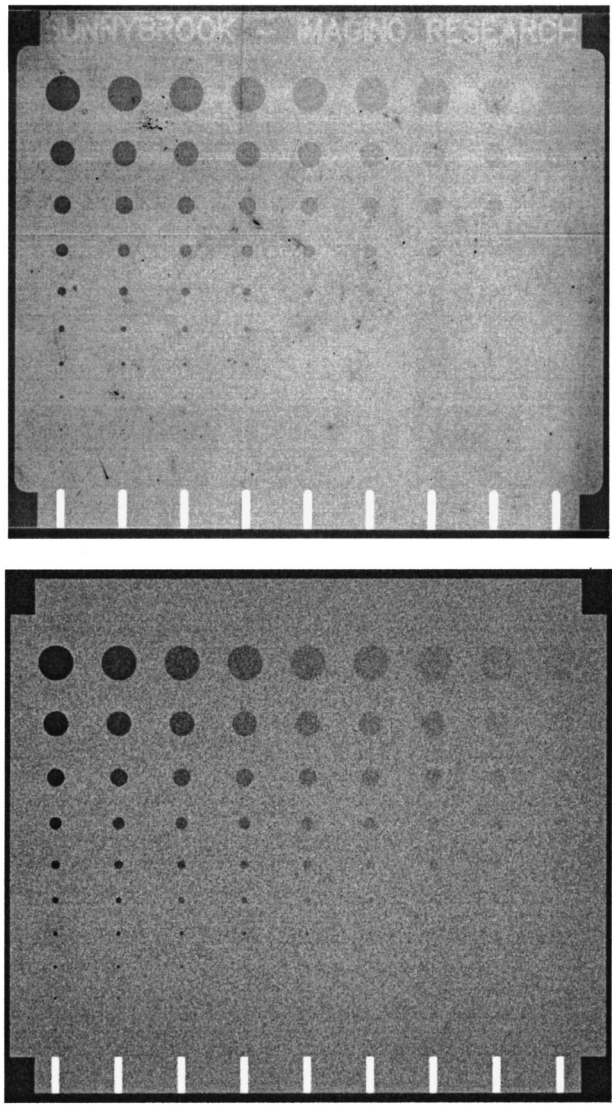

FIG. 6. Images of the contrast detail phantom. Top—real image obtained with the synchrotron system at 18 keV with no collimators. Bottom—Monte Carlo simulation.

VI. METHODS OF COMPARISON

A. Synchrotron imaging

Seven images of each phantom were taken using the X15A synchrotron imaging system at the NSLS. Images were made at 18, 26, 34, and 42 keV. Several collimator sizes were used at 18 keV in order to observe the effects of increased scattered radiation in the image. Noise in the images was typically very low, in the 1% range. The details of each measurement are listed in Table II. The image plates were read by the Fuji BAS2000 using a 100 μm pixel size.

Monte Carlo based simulations were performed with MCMIS for the same conditions as the experimental images from X15A. Pixel size in the fine mesh image was 100 μm and in the coarse mesh image was 0.5 cm. The scatter-to-primary ratios for a 2×2 cm area in the middle of the image as well as over the entire image are listed in Table II. Computing times for the entire Monte Carlo simulations (up to four monoenergetic calculations) are also listed for the Sun Ultra 60 (300 MHz).

B. Fischer Senoscan™

Eight images were taken on the Fischer Senoscan™—five images of the contrast detail phantom at various kVp settings and filters and three images of the ACR phantom using the aluminum filter. Before comparisons to the Monte Carlo images, the Senoscan™ images were reduced in resolution from 54 μm pixel size to 108 μm pixel size. This was only due to the large size of the files and the extra time required to run the Monte Carlo simulations for the smaller pixel size. This did not affect the visibility of any of the items in the images. The parameters of the Senoscan™ images are listed in Table III along with the measured noise level of the reduced images. These values were typically around 0.5%.

Monte Carlo simulations were performed using MCMIS for the same conditions as the Senoscan™ images. Pixel size in each fine mesh image was 100 μm and in the coarse mesh image was 0.5 cm. The scatter-to-primary ratios for a 2×2 cm area in the middle of the image as well as over the entire

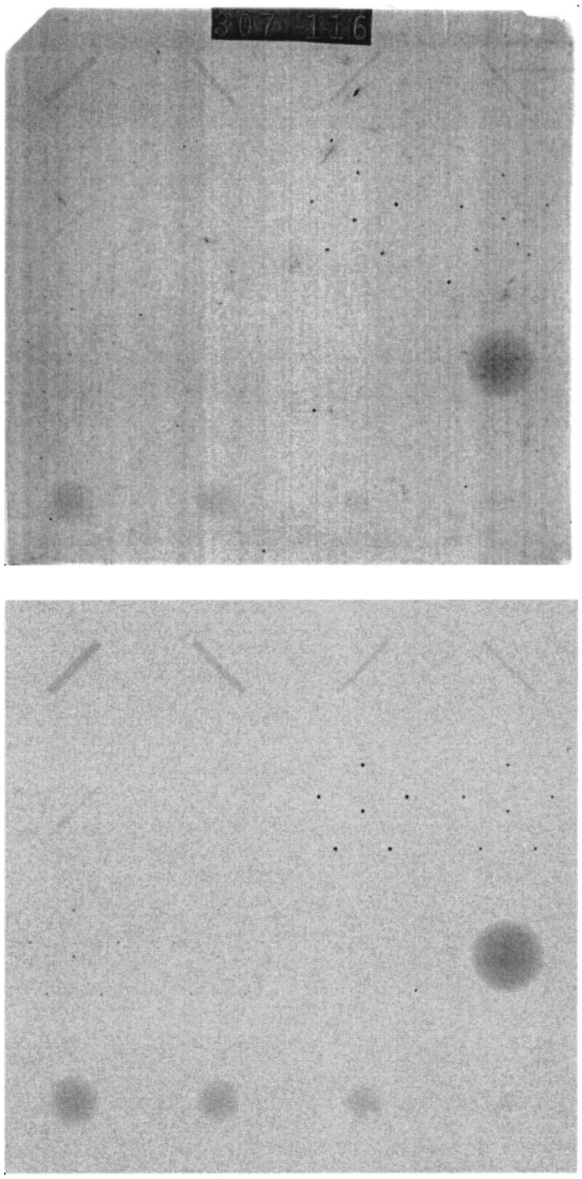

FIG. 7. Images of the ACR phantom. Top—real image obtained with the synchrotron system at 18 keV with 5 mm collimators. Bottom—Monte Carlo simulation.

image are listed in Table III. Computer times are not listed for each image since the same monoenergetic images were used in making the different simulations at different kVp settings and different filters. The total times for all 36 monoenergetic contrast detail phantom images were 12 h for the fine mesh unscattered and 72 h for the coarse mesh scattered images. For the ACR phantom, the total fine mesh unscattered images took 6 h and the coarse mesh scattered images took 99 h. These times are for the Sun Ultra 60.

C. Contrast in the CD phantom

Contrast of an object in the CD phantom is calculated by finding the difference in levels inside and outside of a detail

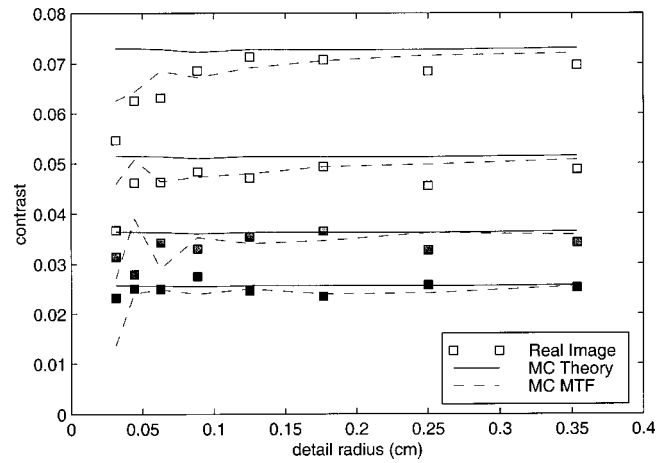

FIG. 8. Contrast of the details in the CD phantom as a function of the detail radius. Each series of points is from a column of details of the same thickness. Data from the real synchrotron image appear as points and the contrast values calculated from the simulated image appear as lines: solid lines from the raw Monte Carlo images and dashed lines after the MTF and noise have been added.

divided by the average level. For example, if the average pixel value inside the detail is a and the average pixel value just outside the detail is b, the contrast c is

$$c=\frac{|a-b|}{\frac{1}{2}(a+b)}. \tag{2}$$

In a perfect imaging system, the contrast would only decrease for thinner details, not for smaller diameter details. In real systems, the decrease in contrast that is observed for smaller objects of the same thickness is due to the scatter component, the MTF of the system, and noise.

VII. RESULTS AND DISCUSSION

A. Synchrotron imaging

Examples of the measured image and the simulated image matching the measurement for both the CD phantom and the ACR phantom are shown in Figs. 6 and 7. Although one image may exhibit a greater degree of darkening than the other in each set, the discernibility of the objects in each phantom is nearly the same in the measured and simulated images, implying that the contrast values of the two images match. The Monte Carlo images are, of course, cleaner because they do not contain the experimental artifacts caused by defects in the monochromators and in the image plate.

For images taken with different collimator sizes, there was no significant change in the observed contrast. The results from MCMIS show average S/P ratios for the center of the CD phantom images of 0.5%, 0.6%, 1.4%, and 4% for the four different collimator sizes of 3 mm, 5 mm, 10 mm and infinite (no collimators) used in the X15A images. Even the image where the S/P was 4%, scatter did not decrease the calculated contrast in the Monte Carlo image. Synchrotron imaging is essentially scatter free and it appears that the analytically calculated unscattered image, with MTF applied and noise, would be sufficient to model the images.

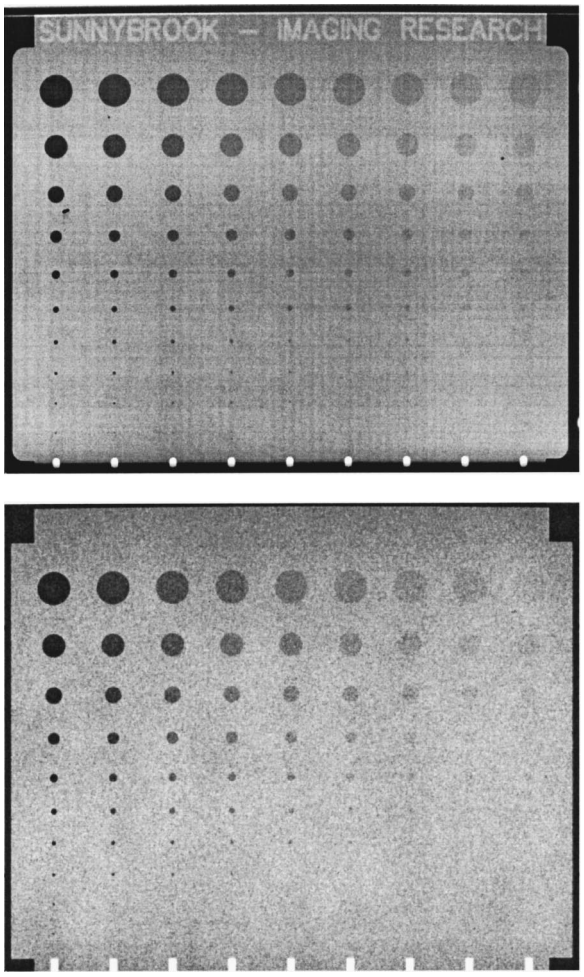

FIG. 9. Images of the contrast detail phantom. Top—real image obtained with the Fischer Senoscan™ at 25 kVp with an aluminum filter. Bottom—Monte Carlo simulation.

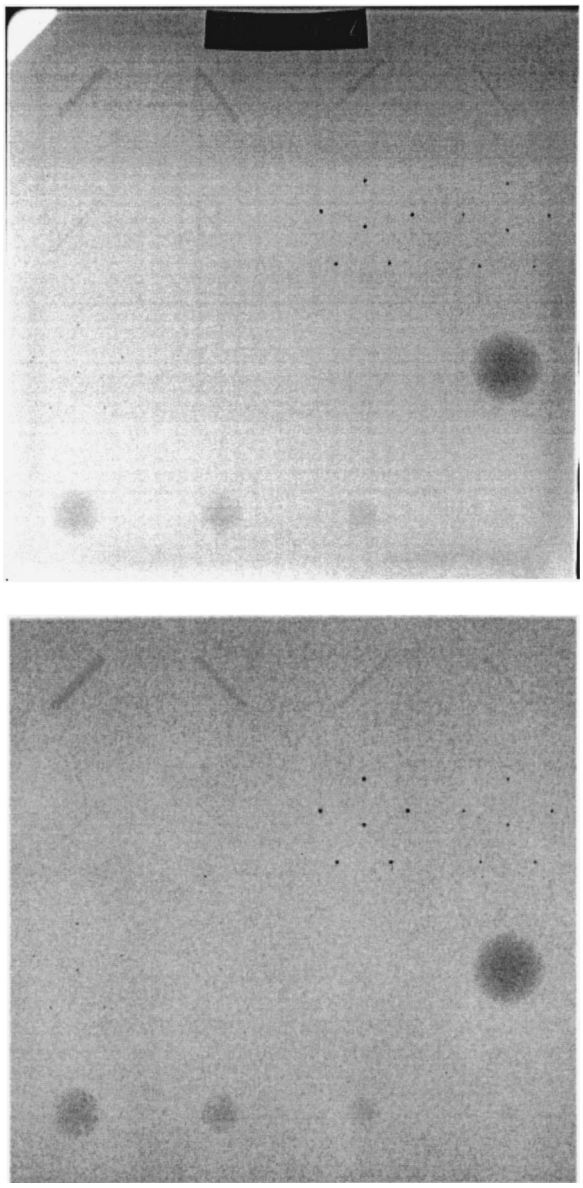

FIG. 10. Images of the ACR phantom. Top—real image obtained with the Fischer Senoscan™ at 30 kVp with an aluminum filter. The nonuniformity of the background is actually very slight—it is enhanced here in the choice of gray scales used to maximize contrast in the image. Bottom—Monte Carlo simulation.

Figure 8 shows the contrast from the first four columns (the same thickness in each column) of the CD phantom shown in Fig. 6. Figure 8 also shows the contrast calculated from the Monte Carlo image before the MTF and noise were applied, and it does not decrease with decreasing detail radius, indicating that the scatter component is small in synchrotron images and only the MTF of the system (image plate and image plate reader) and noise degrades the contrast. The spread in the contrast values for the measured images is mainly due to artifacts in the image. This is more evident for the smaller details, where the averaging is done over fewer pixels.

B. Fischer Senoscan™

The simulations compare very nicely to the real Senoscan™ images. An example of each phantom image taken by the Senoscan™ and its Monte Carlo simulation are shown in Figs. 9 and 10. The simulated images appear very similar to the Senoscan™ images in the level of detail that is visible. One difference between the images is that the amount and type of artifacts in the real Senoscan™ images do not appear in the simulation. The vertical and horizontal stripes in the real image do not appear in the simulation. These stripes are a large part of the calculated noise in the real images but when the same noise level is applied to the simulated images, the same visual appearance is not achieved. The simulated images then appear to have more of a mottled look, and this is one aspect of the simulation that needs improvement. This is also evident in close comparison of the fourth fibril in Fig. 10. This detail is masked by the texture of the noise around it more in the simulated image than the real image.

The computed contrast for the two CD phantom images, as well as the contrast from the Monte Carlo image before the MTF was used (to show contrast degradation from scatter alone) are shown in Fig. 11. Unlike the synchrotron images, the contrast of the Senoscan™ images are slightly degraded

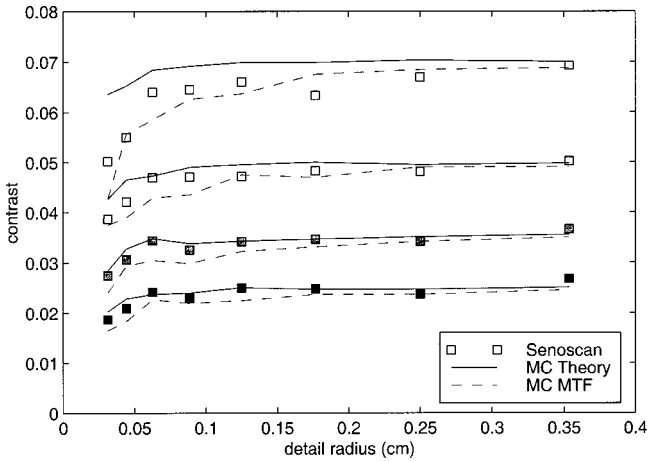

FIG. 11. Contrast of the details in the CD phantom as a function of detail radius. Each series of points is from a column of details of the same thickness. Data from the Fischer Senoscan™ appear as points and the contrast values calculated from the simulated image appear as lines: solid lines from the raw Monte Carlo images and dashed lines after the MTF and noise have been added.

by the scatter contribution (S/P$\sim$9%). Being a scanning slot system, this degradation is still less than in today's conventional mammography units. After applying the MTF to the Monte Carlo image, the calculated contrast matches the contrast measured in the Senoscan™ image fairly well. Since the scatter degrades the contrast, modeling the Senoscan™ does require a calculation of the scatter component.

C. Prospects for simulations

In this paper we have focused on the methods required to perform Monte Carlo calculations for medical images in reasonable amounts of time. To show this, we employed some simple models for including detector response: the MTF of the various simulated systems and system noise. However, use of these simple models does not change the significance of the results, showing that Monte Carlo image simulation can be done in reasonable times and become a very useful tool in the study of mammography systems.

One major difficulty that presents itself is the accurate inclusion of the noise and MTF into the simulation. In real life, noise comes from many parts of the imaging process—from source quantum mottle to electronics. The different contributions to the system MTF also come from many different parts. The difficulty is that these effects on the image are all happening together, at the same time. Including all of these effects at the appropriate time would require very detailed modeling of each photon emitted from the source, as it interacts in the subject, then in the detector, creating a signal that is ultimately segmented into an image. Presently, this would be a very complex and prohibitively time consuming task. As computers expand in capabilities, improvements in all aspects of simulated imaging could be included. For now, our approach of calculating an image using Monte Carlo transport techniques and post-processing by applying the MTF and a simplified noise model seems to be a reasonable compromise, as seen by the good comparisons of real and simulated images.

Noise in the image, especially for the overall 'texture' of the simulations is probably the area that needs the most improvement. The problem for the simulation is that each system will have to be analyzed separately since each has a different combination of physical, electronic, and processing stages leading to noise.

VIII. SUMMARY

Accurate Monte Carlo simulation of complex imaging problems is possible by using a combination of three variance reduction techniques: rastering, point detectors, and the separation of the unscattered and scattered components. Simulated images from two new mammography systems, the Fischer Senoscan™ and the synchrotron based system compared well to real images, both in the level of detail visible in the images and the calculated contrast of standard details. Full 3-D simulation, generating a complete image, should be able to provide more information to system designers compared to simple pencil-beam simulations.

Now that Monte Carlo has been shown to be able to simulate full mammographic images, the opportunity to study different aspects of the imaging system and how they affect the final image is at hand. Monte Carlo gives the analyst the ability to perform experiments not possible in the lab, for example, being able to separate photons scattered from the subject from those scattered in the compression paddle, or whatever else is of interest. Researchers will also be able to determine how material composition information affects the image, just by running different simulations.

One interesting thing that resulted from this study is that the amount of scatter in synchrotron images is so small, scatter can safely be left out of the simulation process. For scanning slot systems like the Fischer Senoscan™, even though the amount of scatter is small compared to conventional mammography systems, the scatter does play an important role in the image formation process and needs to be modeled.

ACKNOWLEDGMENTS

Research was carried out in part at the National Synchrotron Light Source, Brookhaven National Laboratory, which is supported by the U.S. Department of Energy, Division of Materials Sciences and Division of Chemical Sciences. Many thanks to Dr. W. C. Thomlinson and Dr. Z. Zhong for allowing this work to be done on beamline X15A. Dr. R. Eugene Johnston of the University of North Carolina, Chapel Hill, provided assistance in both the synchrotron imaging and Senoscan™ imaging aspects of this study. We thank him for all of his valuable help. Fischer Imaging Corporation supplied a great deal of technical information and help in modeling the Senoscan™. Special thanks to Dr. M. M. Tesic for his time and energy in helping us. Mr. Peplow, a doctoral student at the time this work was done, was supported by Dr. R. Eugene Johnston, UNC-Chapel Hill, through his U.S. Army Medical Research and Material Command Breast Can-

cer Research Grant. He was also supported by a Nuclear Engineering Education Research (NEER) Grant from the Department of Energy, Idaho Operations Office. Monte Carlo development and the analysis of the experimental data were performed on a Sun Ultra 2/200 donated by Sun Microsystems, through their Academic Equipment Grant. Many thanks to Sun Microsystems. Thanks also to the referees whose thorough and thoughtful reviews improved this paper.

[a]Electronic mail: depeplow@eos.ncsu.edu

[1] W. Thomlinson, ''Medical applications of synchrotron radiation at the National Synchrotron Light Source'' in *Synchrotron Radiation in the Biosciences*, edited by B. Chance (Clarendon, Oxford, 1994).
[2] R. Lewis, ''Medical applications of synchrotron radiation x-rays,'' Phys. Med. Biol. **42**, 1213–1243 (1997).
[3] F. Arfelli *et al.*, ''Digital mammography at the Trieste Synchrotron Light Source,'' IEEE Trans. Nucl. Sci. **43**, 2061–2067 (1996).
[4] E. Burattini *et al.*, ''Mammography with synchrotron radiation,'' Radiology **195**, 239–244 (1995).
[5] R. E. Johnston *et al.*, ''Mammographic phantom studies with synchrotron radiation,'' Radiology **200**, 659–663 (1996).
[6] D. Chapman *et al.*, ''Diffraction enhanced x-ray imaging,'' Phys. Med. Biol. **42**, 2015–2025 (1997).
[7] V. N. Ingal, E. A. Beliaevskaya, A. P. Brianskaya, and R. D. Merkurieva, ''Phase mammography—a new technique for breast investigation,'' Phys. Med. Biol. **43**, 2555–2567 (1998).
[8] M. J. Yaffe and J. A. Rowlands, ''X-ray detectors for digital radiography,'' Phys. Med. Biol. **42**, 1–39 (1997).
[9] J. M. Boone and J. A. Seibert, ''Monte Carlo simulation of the scattered radiation distribution in diagnostic radiology,'' Med. Phys. **15**, 713–720 (1988).
[10] H. P. Chan and K. Doi, ''Physical characteristics of scattered radiation in diagnostic radiology: Monte Carlo simulation studies,'' Med. Phys. **12**, 152–165 (1985).
[11] D. R. Dance and G. J. Day, ''The computation of scatter in mammography by Monte Carlo methods,'' Phys. Med. Biol. **29**, 237–247 (1994).
[12] Z. Jing, W. Huda, and J. K. Walker, ''Scattered radiation in scanning slot mammography,'' Phys. Med. Biol. **25**, 1111–1117 (1998).
[13] G. Spyrou, G. Tzanakos, A. Bakas, and G. Panayiotakis, ''Monte Carlo generated mammograms: development and validation,'' Phys. Med. Biol. **43**, 3341–3357 (1998).
[14] G. Panayiotakis (private communication, 1998).
[15] E. C. Snow, ''MCNP™ radiography patch,'' Los Alamos National Laboratory Memorandum No. XTM:96-169(U), 1996.
[16] G. P. Estes and W. M. Taylor, ''Computational radiology and imaging with the MCNP™ Monte Carlo code,'' in *Computational Medicine, Public Health and Biotechnology: Building a Man in the Machine*, edited by M. Whitten (World Scientific, River Edge, NJ, 1995), pp. 832–845.
[17] J. A. Halbleib, R. P. Kensek, T. A. Mehlhorn, G. D. Valdez, S. M. Seltzer, and M. J. Berger, *ITS Version 3.0: The Integrated TIGER Series of Coupled Electron/Photon Monte Carlo Transport Codes*, SAND91-1634 (Sandia National Laboratories, Albuquerque, NM, 1992).
[18] J. H. Hubbell and I Øverbø, ''Relativistic atomic form factors and photon coherent cross sections,'' J. Phys. Chem. Ref. Data **8**, 69–105 (1979).
[19] D. E. Peplow and K. Veghese, ''Measured molecular coherent scattering form factors of animal tissues, plastics and human breast tissue,'' Phys. Med. Biol. **43**, 2431–2452 (1998).
[20] M. Tesic (private communication, 1998).
[21] D. E. Peplow, ''Monte Carlo mammography image simulation with measured coherent scattering form factors and differential sampling,'' Doctoral dissertation at North Carolina State University, available through UMI (Bell & Howell), 1999.
[22] J. M. Boone, ''Parameterized x-ray absorption in diagnostic radiology from Monte Carlo calculations: implications for x-ray detector design,'' Med. Phys. **19**, 1467–1473 (1992).
[23] B. Liu, M. Goodsitt, and H. P. Chan, ''Normalized average glandular dose in magnification mammography,'' Radiology **197**, 27–32 (1995).
[24] C. J. Leliveld, J. G. Maas, V. R. Bom, and C. W. E. van Eijk, ''Monte Carlo modeling of coherent scattering: influence of interference,'' IEEE Trans. Nucl. Sci. **43**, 3315–3321 (1996).
[25] Z. Zhong (private communication, 1998).
[26] International Commission on Radiation Units and Measurements, ''Modulation transfer function of screen-film systems,'' Report 41, 1986, p. 21.
[27] J. M. Boone, T. R. Fewell, and R. J. Jennings, ''Molybdenum, rhodium, and tungsten anode spectral models using interpolating polynomials with application to mammography,'' Med. Phys. **24**, 1863–1874 (1997).